The European Physical Journal Plus

Conservation state of cast iron metalworks in European street furniture

--Manuscript Draft--

Manuscript Number:	EPJP-D-18-01380R2
Full Title:	Conservation state of cast iron metalworks in European street furniture
Article Type:	FP: Past and Present: Recent Advances in the Investigation of Ancient etc
Corresponding Author:	Chiara Soffritti University of Ferrara ITALY
Corresponding Author Secondary Information:	
Corresponding Author's Institution:	University of Ferrara
Corresponding Author's Secondary Institution:	
First Author:	Chiara Soffritti
First Author Secondary Information:	
Order of Authors:	Chiara Soffritti
	Laura Calzolari
	Andrea Balbo
	Federica Zanotto
	Cecilia Monticelli
	Francesca Ospitali
	Annalisa Fortini
	Gian Luca Garagnani
Order of Authors Secondary Information:	
Funding Information:	
Abstract:	This work evaluates the state of conservation of three artefacts of historical street furniture in cast iron, dating back to the second half of the nineteenth century and coming from foundries located in Italy, France and Great Britain. Form, distribution and size of graphite in cast irons, and the constituents of microstructures were evaluated by optical microscopy, whereas the alloy composition was determined by scanning electron microscopy with energy dispersive spectroscopy (SEM/EDS). The same analytical technique, in association with Diffuse Reflectance Infrared Fourier Transform (DRIFT) and micro-Raman spectroscopies, was employed to characterize corrosion attack morphology, patina stratification and thickness. The protectiveness of the corrosion layers on the artefacts was evaluated by Electrochemical Impedance Spectroscopy (EIS). The results showed that the microstructure and alloy composition were similar to those frequently encountered in complex shape castings with variable wall thickness. On the corroded surfaces, the graphitization of the cast irons was detected. This phenomenon was accompanied by the deposition of corrosion layers of variable thickness, containing iron oxides, oxy-hydroxides, chlorides and silicon oxides. The corrosion layers of most artefacts showed a poor protectiveness, particularly when they included chlorides, detected in association with akaganeite among corrosion products.

To the Guest Editors of

The European Physical Journal Plus

Subject: Revision of manuscript EPJP-D-18-01380R1

Dear Sirs,

Thank you very much for your mail and for kindly providing comments and/or suggestions on our manuscript (EPJP-D-18-01380R1). We carefully amended the manuscript according to the suggestions provided and enclose a detailed answer to the Reviewers' comments. We hope now that the manuscript is suitable for publication on your Journal.

Thank you for your kind attention and best regards,

Chiara Soffritti, PhD
Corresponding author

Department of Engineering
University of Ferrara,
Via Saragat 1, 44122 Ferrara (Italy)
E-mail: chiara.soffritti@unife.it

Ferrara, April 26th, 2019

ANSWERS TO THE REVIEWERS:

REVIEWER #2

The authors have improved the manuscript, but some points should be enhanced. I suggest evaluating the publication after clarification of some critical issues concerning especially the electrochemical section. Please indicate pages and lines in the answers, not just using the highlighter, when making changes in the text.

Introduction:

- The authors added information and bibliography about the use of SEM / EDS, FTIR and Raman. In this way there is an imbalance in the literature review carried out in the introduction. I suggest introducing also the use of EIS for metals of Cultural Heritage, as it is a technique used by the authors in the work, in the same way as the others already mentioned. There are many pivotal works published in the last few years about impedance measurements carried out by the authors.

As suggested by the Reviewer, the *Introduction* was modified by expanding the section dedicated to EIS measurements in the field of cultural heritage (**page 3 lines 1-15**).

Experimental:

- Usually the aims and the explanation of the use of certain techniques for solving a problem are added at the end of the introduction (when a dedicated section missing). In the experimental part there must be only information about the instruments used. I therefore suggest moving especially the sentence on page 3 line 42 in the final part of the introduction and possibly discussing in this context the usefulness of the joint use of DRIFT and micro raman.

Following the Reviewer's suggestion, the sentence was moved to the *Introduction* and included in the discussion (**page 3 lines 19-24**).

- In the recent literature on EIS analysis on metals of cultural interest when using mineral water, the composition and origin of the water itself is also indicated. This makes possible the reproducibility of the experiment in the same conditions and using the same electrolyte (in this case a cloth soaked with a natural mineral water). I therefore suggest that you include this important information.

Information about the mineral water used in the EIS measurement were added in section *2 Experimental* (**page 4 lines 4-7**).

Results and discussion: 3.3 Electrochemical characterization

- Please take care of the Bode representation: in a Bode plot, conventionally used in the electrochemical research, log|Z| and φ are both plotted vs. logω. Modify the plot showed in Fig.9 of the revised version. Moreover, the frequency scale ends at 1.10 105 while in the text is declared that the EIS measurement was carried out between 1MHz - 1 mHz frequency range (page 3 line 57 of the revised version). Furthermore, log|Z| can be an important indicator of the corrosion degree of the artefacts and it is more reliable than the considerations taken from the fitting with the equivalent circuits. I suggest considering this side, important in EIS studies, and to review the literature about it.

As far as the frequency range of EIS spectra reported in section *2 Experimental*, the Reviewer correctly observed that it is larger than that reported in the spectra of Fig. 9. In particular, the highest frequency decade (frequencies higher than 10^5 Hz) was omitted because it showed the system inductive response, due to instrument, electrode or connecting wire artefacts [E. Barsoukov, J.R. Macdonald, Impedance Spectroscopy Theory, Experiment, and Applications, Second Edition, Wiley Interscience, John Wiley & Sons, Inc., Hoboken, New Jersey (2005); J.R. Scully, D.C. Silverman, M.W. Kending, Electrochemical Impedance Analysis and Interpretation, STP 1188 ASTM (1993)]. The lowest frequency decade (usually below 10 mHz) was affected by scattering and scattered data were also omitted, so that the lowest significant frequencies were those reported in Fig. 9.
According to the Reviewer's suggestion, Fig. 9 was modified with the addition of log |Z| vs. log f Bode plot. As evidenced in literature [B. Ramirez Barat, E. Cano, In Situ Electrochemical Impedance Spectroscopy Measurements and their Interpretation for the Diagnostic of Metallic Cultural Heritage: A Review. ChemElectroChem 5 (2018) 2698-2716], log |Z| at a sufficiently low frequency (e.g. 10 mHz) can be a useful parameter for comparative studies on different patina-substrate or corrosion products layer-substrate systems, especially in the presence of particularly noisy spectra or different phenomena overlapping, which make a reliable fitting with an appropriate equivalent circuit (EC) quite difficult. We have instead performed the analysis of the EIS spectra by fitting them with an EC which interprets the experimental data on the basis of a simple physical model (electrode covered by a porous film of corrosion products, where the substrate corrosion involves a diffusion step and a charge transfer process at the bottom of the film pores), largely documented and accepted by other authors [L. Bousselmi, C. Fiaud, B. Tribollet, E. Triki, The Characterisation of the Coated Layer at the Interface Carbon Steel-Natural Salt Water by Impedance Spectroscopy, Corrosion Science 39 (9) (1997) 1711-1724; M. Sancy, G. Yannick, E.M.M. Sutter, B. Tribollet, Mechanism of Corrosion of Cast Iron Covered by Aged Corrosion Products: Application of Electrochemical Impedance Spectrometry, Corrosion Science 52 (4) (2010) 1222-1227; E. Angelini, D. Assante, S. Grassini, M. Parvis, EIS Measurements for the Assessment of the Conservation State of Metallic Works of Art, International Journal of Circuits, Systems and Signal Processing 8 (2014) 240-245]. This method gives more information about the corrosion mechanism and affords suggestions about the best strategies to reduce corrosion rates.

- It is somewhat surprising that it is possible to fit three very different spectra with the same equivalent circuit. Especially for Dublin sample, the only one that would seem to show the resistance to the mass transfer and diffusive constrains justifying the use of a Warburg element. So you should explain why you can fitting everything with a single equivalent circuit. The goodness of the fitting is not shown.

Taking into consideration the processes that can presumably occur on iron exposed to the atmosphere, we used the EC reported in Fig. 10 (quite similar to that used by [L. Bousselmi, C. Fiaud, B. Tribollet, E. Triki, The Characterisation of the Coated Layer at the Interface Carbon Steel-Natural Salt Water by Impedance Spectroscopy, Corrosion Science 39 (9) (1997) 1711-1724; M. Sancy, G. Yannick, E.M.M. Sutter, B. Tribollet, Mechanism of Corrosion of Cast Iron Covered by Aged Corrosion Products: Application of Electrochemical Impedance Spectrometry, Corrosion Science 52 (4) (2010) 1222-1227; E. Angelini, D. Assante, S. Grassini, M. Parvis, EIS Measurements for the Assessment of the Conservation State of Metallic Works of Art, International Journal of Circuits, Systems and Signal Processing 8 (2014) 240-245]), which describes the behavior of a metal substrate covered by a porous film of corrosion products, where the substrate corrosion involves a diffusion step and a charge transfer process at the bottom of the film pores. This involves three time constants (related to the dielectric properties of the surface film, the charge transfer at the bottom of the film pores and the diffusion process through the pores) which can be distinguished in the phase angle vs. frequency Bode plots of Dublin and Palermo samples, less clearly in Florence sample (Fig. 9-c). In all cases, however, the EIS fitting largely improves if all three time constants are considered. The limited visibility of one time constant may occur because the electrochemical response of the studied systems may be influenced to a different extent by the three considered contributes to the whole corrosion process. The parameters obtained from the fitting evidenced that the better conservation state of Dublin sample is due to a slow charge transfer and hindered diffusion process through a relatively homogeneous compact patina, in comparison to Florence and Palermo samples. The considered EC fits quite well all the three EIS spectra as evidenced by the χ^2 parameter (now added in table 5), which assess the good quality of the fitting.

In EIS studies, it is a common approach the adoption of a proper EC (related to a suitable physical model) which improves the fitting and the comprehension of the studied system even if not all time constants included in the EC are always clearly evident in the spectra [W. Qafsaoui M.W. Kendig, H. Perrot, H. Takenouti, Coupling of Electrochemical Techniques to Study Copper Corrosion Inhibition in 0.5 mol L^{-1} NaCl by 1-Pyrrolidine Dithiocarbamate, Electrochimica Acta 87 (2013) 348–360; K. Marusic, H. Otmacic-Curkovic, S. Horvat-Kurbegovic, H. Takenouti, E. Stupnisek-Lisac, Comparative Studies of Chemical and Electrochemical Preparation of Artificial Bronze Patinas and Their Protection by Corrosion Inhibitor, Electrochimica Acta 54 (2009) 7106–7113; I. Rotaru, S. Varvara, L. Gaina, L.M. Muresan, Antibacterial Drugs as Corrosion Inhibitors for Bronze Surfaces in Acidic Solutions, Applied Surface Science 321 (2014) 188–196].

Conservation state of cast iron metalworks in European street furniture

Chiara Soffritti[1*], Laura Calzolari[1], Andrea Balbo[1], Federica Zanotto[1], Cecilia Monticelli[1], Francesca Ospitali[2], Annalisa Fortini[1], Gian Luca Garagnani[1]

[1] "A. Daccò" Corrosion and Metallurgy Study Centre, Engineering Department, University of Ferrara, Via Saragat 4a, I-44122 Ferrara, Italy

[2] Industrial Chemistry Department "Toso Montanari", University of Bologna, Viale del Risorgimento 4, I-40136 Bologna, Italy

[*] Corresponding author
"A. Daccò" Corrosion and Metallurgy Study Centre
Department of Engineering
University of Ferrara
Via Saragat 4a, I-44122 Ferrara, Italy
Tel. +39 0532 974843
Fax +39 0532 974870
e-mail: chiara.soffritti@unife.it

Co-authors addresses: laura.calzolari@student.unife.it, andrea.balbo@unife.it, federica.zanotto@unife.it, mtc@unife.it, francesca.ospitali@unibo.it, annalisa.fortini@unife.it, gian.luca.garagnani@unife.it

Abstract

This work evaluates the state of conservation of three artefacts of historical street furniture in cast iron, dating back to the second half of the nineteenth century and coming from foundries located in Italy, France and Great Britain.

Form, distribution and size of graphite in cast irons, and the constituents of microstructures were evaluated by optical microscopy, whereas the alloy composition was determined by scanning electron microscopy with energy dispersive spectroscopy (SEM/EDS). The same analytical technique, in association with Diffuse Reflectance Infrared Fourier Transform (DRIFT) and micro-Raman spectroscopies, was employed to characterize corrosion attack morphology, patina stratification and thickness. The protectiveness of the corrosion layers of the artefacts was evaluated by Electrochemical Impedance Spectroscopy (EIS).

The results showed that the microstructure and alloy composition were similar to those frequently encountered in complex shape castings with variable wall thickness. On the corroded surfaces, the graphitization of the cast irons was detected. This phenomenon was accompanied by the deposition of corrosion layers of variable thickness, containing iron oxides, oxy-hydroxides, chlorides and silicon oxides.

The corrosion layers of most artefacts showed a poor protectiveness, particularly when they included chlorides, detected in association with akaganeite among corrosion products.

Keywords: Street furniture; Cast iron; Microstructure; Graphitization; Micro-Raman; DRIFT Spectroscopy; EIS

1 Introduction

In the literature, street furniture was firstly defined by the urbanist Baron Haussman (Prefect of Paris, France, from 1853 to 1870 CE) as 'the group of objects or accessories which, installed in the urban space, performs a functional service for the community'. Bassi Neri and Bazzocchi [1] further remarked that 'safety, hygiene, comfort and entertainment were the requirements of the nascent bourgeoisie, and the modern city needed to respond to them. The city layout changed radically in those years, making it possible to introduce new purposely-created elements'. Thus, street furniture was a class of objects created to improve the quality of life in urban settlements, which has evolved with the human necessities during years, and nowadays is an integral part of the city. Street lamps, balconies, grids, benches, fountains and gazebos are only some of the elements that compose the whole category and which have an ancient origin [2].

The massive diffusion of street furniture composed of cast iron alloys was mainly due to the technological progress achieved in the iron and steel industry during the Industrial Revolution (1760-1840 CE). Over the second half of the nineteenth century and the first decades of the twentieth century, cast iron was widely used for urban décor and non-load-bearing architectural elements, while wrought iron was preferred for load-bearing structures. However, street furniture was not exclusively made of cast iron: other materials were also employed, such as concrete for street lamps and stone for balconies and grids [3].

The safeguard of cast iron artefacts with relevant archaeological and historical interest from atmospheric corrosion is an important problem, because they are often exposed to aggressive environments, such as urban atmosphere in modern cities. Nevertheless, only a few studies were carried out on this phenomenon, so that the quantitative data and information about the corrosion behavior of cast irons are relatively scarce, in comparison to steels [4,5]. It is reported that the long-term corrosion rate of cast irons exposed outdoor is lower than that of mild steel, especially in atmospheres with high concentrations of pollutants because of the formation of protective layers, acting as a barrier against the corrosion progress [6].

The nature and the growth rate of the corrosion layers at the surface / electrolyte interface depends on many factor such as the alloy composition, temperature, relative humidity (RH), time of wetness (TOW), wind exposure and velocity, dew and fog [6,7]. The corrosion rate is usually very low at RH lower than 65%, whereas a RH higher than 70% induces a generalized corrosion attack in unalloyed cast irons [3].

Air pollutants, such as SO_2, NO_x and chloride-containing particulate matter strongly increase the corrosion rate as they partially dissolve in the surface electrolyte film, increasing its electrical conductivity and reducing the protectiveness of surface patinas [8]. The initial corrosion rate of cast irons varies from values lower than 25 μm/y in a pollution-free rural atmosphere to over 150 μm/y in a polluted atmosphere containing SO_2 or sea-salt spray aerosol particles. These corrosion rates decrease with increasing the exposure time, due to the formation of an adherent and protective corrosion patina [6,8].

The surface rust layer can be quite complex but usually two main stratifications can be distinguished: the inner layer, formed by selective attack of the ferrous matrix, contains the corrosion-resistant phases, like graphite, phosphorous eutectic and carbide eutectic. The layer porosity is sealed by the corrosion products (iron oxides, oxy-hydroxides and oxidation products of silicon and phosphorous) and the resulting compact and adherent protective deposit acts as a protective barrier that hinders the corrosion process. The outer layer mainly contains corrosion products, similar to the ones that can usually be found on steels and appear voluminous and porous. In polluted atmospheres, it may also contain sulfates, basic sulfates, chlorides and nitrates [9,10].

Therefore, the analyses of the corrosive attack morphology, composition and stratification of corrosion products is particularly useful to gain an insight on the conservation state of cast iron artefacts and on the aggressiveness of the environment in which they were exposed.

In this regard, the SEM/EDS, FTIR and Raman techniques were particularly suitable to analyze iron corrosion products developed on the surface of metallic artefacts under atmospheric conditions or aqueous conditions [11-14]. In fact, by SEM/EDS it is possible to study the composition of the corrosion layers and the distribution of the alloying elements or aggressive species in the corrosion products. FTIR and Raman spectroscopy can identify the various forms of iron oxides / oxyhydroxides and other corrosion products (both amorphous or crystalline) providing information about the stratification and the evolutions of the corrosion products layers [15-17].

Beside the study of surface patina morphology and nature, the development of suitable conservation strategies for metallic artefacts exposed outdoors also requires a close investigation of the corrosion process. Gravimetric methods [18,19] need microsampling carried out by mechanical methods, which disregard the integrity and aesthetical appearance of the object. Moreover, they provide integrated and not instantaneous information on the rate of the corrosion processes. Atmospheric corrosion monitors (ACM) [20] and some types of impedance-based sensors [21] are useful to collect information about the aggressiveness of the environment, but do not

give direct information on the ongoing corrosion process. On the contrary, the electrochemical impedance spectroscopy (EIS) is a consolidate technique largely used in corrosion science to study the corrosion mechanisms [22,23] and to investigate the effectiveness of protection measures including corrosion inhibitors and coatings [24-26].

In the field of cultural heritage, this technique has been increasingly used mainly because it has the great advantage to be a non-destructive technique capable to preserve the artifacts surface even in the presence of a pre-existing patina. It allows the assessment of the artifact conservation state, the comparison of protective coating effectiveness and their monitoring during long exposure periods, often by simply evaluating parameters such as the impedance module at a low frequency, e.g. 10 mHz [27,28] or the polarization resistance value obtained by fitting methods as the low frequency limit of the electrochemical impedance at frequency tending to 0 Hz [29-32]. However, the technique is a powerful diagnostic tool for researchers and conservators often applied in field and capable of a deep investigation of corrosion and corrosion protection mechanisms by analyses of EIS spectra fitting parameters [28,31,33,34]. Recently, in situ EIS was successfully applied for diagnostic purposes on bronze and steel artifacts exposed outdoor by using specifically developed electrochemical cells or contact probes [28,35-41].

The present study investigates the conservation state of three objects of historical street furniture in cast iron, dating back to the second half of nineteenth century and coming from foundries located in Italy, France and Great Britain. The results of investigations on the alloys microstructure and chemical composition are presented. Microstructural features are studied to assess the manufacturing procedures. The nature of corrosion products was characterized through FTIR analyses while micro-Raman measurements were carried out in order to elucidate patina stratification.

The information obtained from the corrosion attack characterization, surface patina composition and morphology were integrated by the results of EIS spectra analysis, in order to better clarify the corrosion process and the patina protectiveness.

2 Experimental

In order to preserve the artefacts from further damage, most of the investigations were performed on fragments, detached from the objects. Fragments are shortly described in Table 1, together with information on origin, year of manufacturing and nationality of the foundry.

The chemical composition and microstructure of the alloys were determined on cross sections of the samples (samples observed across the thickness of the metal) and from the longitudinal sections (samples observed in the direction of the metal surface). The samples were embedded in mounting resin, polished, degreased in acetone, dried and stored in a desiccator. The analyses of the cast irons microstructure before chemical etching were performed by a Leica MEF4M optical microscope (OM) (Leica, Wetzlar, Germany), to determine the form, distribution and size of graphite, in accordance with the standard EN ISO 945-1:2008. The microstructure after chemical etching with Nital 4 (4% nitric acid in ethanol) was analyzed by optical microscopy and scanning electron microscopy operating in variable pressure conditions (VPSEM). The scanning electron microscope was a Zeiss EVO MA 15 (Zeiss, Oberkochen, Germany) with an Oxford X-Max 50 (Oxford Instruments, Abingdon-on-Thames, UK) energy dispersive microprobe for semi-quantitative analyses (EDS). Analyses of unetched polished cross sections were carried out by VPSEM/EDS to evaluate alloys composition.

Samples in cross section and in unetched conditions were also used to investigate the thickness of the patina and the stratification of corrosion products by VPSEM/EDS. The operating parameters were 20 kV acceleration voltage, in air atmosphere at a 50 Pa pressure. For each sample, the thickness of the patina was an average of 10 measurements.

The corrosion products were analyzed by Fourier Transform Infrared (FTIR) spectroscopy with a Thermo-Scientific Nicolet iS50 spectrometer (Thermo Fisher Scientific, Waltham, USA). Because of the irregular geometry of post surfaces, the corrosion products were collected from surface by grinding with potassium bromide and then analyzed with the DRIFT (Diffuse Reflectance Infrared Fourier Transform) accessory. During the analyses, the spectrometer was purged with dry, CO_2-free air generated with a Balston 75-52 unit and a deuterated triglycine sulfate (DTGS) detector was used to investigate the region from 4000-400 cm^{-1} with a resolution of 4 cm^{-1}.

The corrosion product stratification was analyzed by micro-Raman spectroscopy on sample cross sections, obtained with traditional metallographic techniques. This analysis was carried out with a micro-Raman spectrometer Invia (Renishaw Wotton-under-Edge, UK) equipped with a laser diode with λ = 782 nm (laser

beam spot size < 2 μm). The spectra were obtained by collecting 4 scans (t_{sca} = 10 s) for each spectrum and by using an output power of 3 mW.

The corrosion behavior of post samples was evaluated in laboratory by Electrochemical Impedance Spectroscopy (EIS). The tests were carried out by using an EIS probe, similar to that already used in [38,42], placed in contact with the sample surface by interposing a cloth soaked with a commercial natural mineral water (conductivity Λ = 222 μS·cm^{-1} at 20 °C, composition: Na^+ 1.0 mg/l, K^+ 0.2 mg/l, Ca^{2+} 19.6 mg/l, Mg^{2+} 4.1 mg/l, Cl^- < 2 mg/l, HCO_3^- 76 mg/l, SO_4^{2-} 3.0 mg/l). The Saturated Calomel Electrode (SCE) was used as a reference during the measurements. The spectra were recorded after about 20 min monitoring of the open circuit potential (E_{OCP}), when the E_{OCP} variations were lower than 2 mV/10 min. For these tests, a PAR EG&G 273A potentiostat (Princeton Applied Research, Princeton, USA) was used, coupled with a FRA Solartron 1260 frequency response analyzer (Ametek, Berwyn, USA), under the following experimental conditions: ±10 mV rms alternating potential signal; 100 kHz – 1 mHz frequency range.

3 Results and discussion

3.1 Alloy microstructure and chemical composition

The optical micrographs of the microstructure observed on the cross sections of cast irons before chemical etching are shown in Figs. 1(a-c). All samples can be classified as gray cast iron [43]. In accordance with the standard EN ISO 945-1:2008, the sample 1_Florence (Fig. 1a) was characterized by: (i) 70% lamellar graphite of Type A (apparently uniform distribution) and size 4 (graphite lamellae between 0.12 and 0.25 mm in length); (ii) 30% lamellar graphite of Type C (aggregate of larger graphite flakes surrounded by smaller, randomly oriented graphite flakes) and size 4. The sample 2_Dublin (Fig. 1b) contained lamellar graphite of Type B (rosette grouping with random orientation) and size 6/7 (lamellae lengths in the range of 0.015 and 0.060 mm). Finally, the sample 3_Palermo (Fig. 1c) was characterized by: (i) 80% lamellar graphite of Type B and size 5; (ii) 20% lamellar graphite of Type D (fine, randomly oriented graphite flakes in the interdendritic position) and size 8 (lamellae lengths shorter than 0.015 mm).

It is known that form, size and distribution of graphite are strongly related to the cooling rates, degree of undercooling, cast additives and impurities, inoculation and overheating of the melt [43]. For our artefacts, no information is available about their manufacturing techniques. On the other hand, the Type A lamellar graphite of the sample 1_Florence, suggests a low to intermediate degree of undercooling and / or a sufficient inoculation treatment [43,44]. For the samples 2_Dublin and 3_Palermo, the Type B lamellar graphite indicates an alloy solidified with an intermediate degree of undercooling. As prescribed by the standard EN ISO 945-1:2008, this Type B lamellar graphite is associated with the Type D lamellar graphite, which forms typically under a higher degree of undercooling [43,44].

The optical micrographs of the microstructure observed on the cross sections of cast irons after chemical etching are shown in Figs. 1(d-f). The microstructure of the sample 1_Florence was pearlitic with ferrite, traces of steadite (eutectic of iron phosphide Fe_3P and iron) and impurities in the form of polygonal shape particles (Fig. 1d). Polygonal shape particles were identified as manganese sulfide inclusions by semi-quantitative VPSEM/EDS analyses. Differently to steels, where manganese sulfide inclusions are intentionally obtained to improve machinability, cast irons show these inclusions as a natural result of the foundry process [45]. The microstructure of the sample 2_Dublin was ferritic, with pearlite, steadite and distributed inclusions of manganese sulfide (Fig. 1e), whereas the microstructure of the sample 3_Palermo was characterized by the presence of pearlite, ferrite close to the graphite rosettes, steadite and manganese sulfide inclusions (Fig. 1f).

The semi-quantitative elemental composition of the alloys in the artefacts measured by VPSEM/EDS is reported in Table 2. All artefacts were composed of ferrous alloys with silicon (2.0÷3.0 wt.% for samples 2_Dublin and 3_Palermo, ≈1.0 wt.% for sample 1_Florence), phosphorous (1.0÷1.5 wt.% for samples 2_Dublin and 3_Palermo, ≈0.10 wt.% for sample 1_Florence), manganese (0.10÷0.60 wt.% for samples 1_Florence and 2_Dublin, ≈1.7 wt.% for sample 3_Palermo), sulfur (0.10÷0.40 wt.%) and titanium (0.05÷0.20 wt.%).

Silicon and manganese are the most common alloying elements of cast irons. Concerning silicon, a generally accepted theory is that introduction of silicon and its dissolution into liquid iron contribute to the formation of graphite [46,47]. In the studied alloys, it always appears uniformly distributed. Manganese is dissolved in solid solution and also forms manganese sulfide inclusions in the form of polygonal shape particles [43].

All samples showed microstructures with more or less significant steadite contents due to the addition of phosphorous. This element lowers the melting point and improves the fluidity of cast iron alloys, making it possible to create nearly unlimited decorative and structural elements with thin wall thickness (*e.g.* castings

for European street furniture similar to the examined artefacts) [7,9,42,48]. It means that elements made of cast iron are very uniform in appearance and are frequently prepared repetitively.
Titanium is a trace element that modifies graphite nucleation and growth. As confirmed by our optical microscope observations, an increase in the amount of titanium promotes the undercooling of graphite [49], changing the distribution of graphite from Type A (sample 1_Florence, Fig. 1a) to Type D (sample 3_Palermo, Fig. 1c).

3.2 Characterization of the corrosion phenomena

The VPSEM micrographs of the corroded surfaces of cast irons are showed in Figs. 2(a-c). All artefacts were covered by a patina of corrosion products, with rather irregular thickness and semi-quantitative surface elemental composition as reported in Table 3.
The corrosion products of sample 1_Florence contained chlorine (about 0.60%) and lower amounts of silicon, phosphorous and sulfur in comparison to the other samples, in agreement with the lower content of these elements in the metal substrate. A limited amount of calcium was detected, coming from particulate matter. In fact, wind-transported soil dust particles usually rich in aluminum, silicon, calcium, potassium and titanium can be easily incorporated in surface patinas exposed to the atmosphere [6,50,51].
On the patinas of samples 2_Dublin and 3_Palermo almost no chlorine was detected. For these samples, other contaminant elements were identified, *i.e.* potassium and aluminum again originated by atmospheric particulate pollution. Finally, the corrosion products of samples 2_Dublin and 3_Palermo contained zinc and lead, as residues of paint layers for the corrosion protection.
The VPSEM backscattered electron images of the corrosion patina in cross section are shown in Figs. 3(a-c) and permit to investigate the patina stratigraphy. The mean thickness of the corrosion patinas of samples 1_Florence (Fig. 3a) and 3_Palermo (Fig. 3c) was similar (between 115 and 130 μm, as measured by VPSEM/EDS). For these samples, the patinas were irregular with many microcracks occurring perpendicularly and / or parallel to the corroded surfaces. In sample 1_Florence, graphite lamellae intermixed with the corrosion products were also observed throughout the patina thickness. Concerning the corrosion patina of the sample 2_Dublin (Fig. 3b), it was more compact and less irregular than the other patinas, with mean thickness of about 40 μm, again evaluated by VPSEM/EDS. However, some microcraks were visible also in this case.
The VPSEM/EDS element mapping of the corrosion layers on the cross sections of the examined samples is presented in Fig. 4. For all samples, the iron, oxygen, silicon and phosphorous distributions indicated the presence of two distinct corrosion layers in agreement with previous research findings [6,9,10]. They are the result a specific corrosion phenomenon named ‘graphitization’. In fact, in outdoor environments, acidic rainwater selectively corroded the iron matrix of cast irons, then the electrochemically nobler graphite further promoted the attack of the surrounding metal by galvanic coupling effect. Consequently, a corrosion layer, which had no equivalent in steel and exactly occupying the volume of the original metal, was observed and indicated by the letter A in the electron image at the lower left corner of Fig. 4. This inner layer, referred to as ‘topotaxial layer’ or ‘graphitic corrosion residue’ in the literature [6,7,9,42], contained the graphite lamellae, as an interlinked three-dimensional network, and the inert, non-corroded elements of cast irons (especially, the eutectic of iron phosphide Fe_3P and iron). The pores resulting from the selective attack of the matrix were partially replenished by iron corrosion products (iron oxides and oxy-hydroxides for all samples, and iron chlorides in the case of sample 1_Florence). Additionally, oxidation products of silicon (e.g. silicic acid [6,7,9,42]) were detected in sample 2_Dublin and 3_Palermo, where the selective dissolution of iron close to graphite lamellae left a significant silicon enrichment. The outer layer (indicated by the letter B in the electron image at the lower left corner of Fig. 4), often named epitaxial layer’, grew on the artefact surface as a result of surface reaction of iron ions with the aggressive species in the environment and, as already reported, incorporated contamination elements [6,7,9,42].
Figure 5 shows the DRIFT spectra of the corrosion products collected from the studied post surfaces. These corrosion products were obtained by scraping relatively large surfaces, close to the areas tested by EIS. They are representative of the all patina thickness and therefore do not afford information about the corrosion product stratigraphy.
All spectra showed the characteristic peaks of lepidocrocite (γ-FeOOH) at 1022, 740 and 471 cm^{-1} and goethite (α-FeOOH) at 886 and 797 cm^{-1}, related to the in-plane and out-of-plane Fe-O-H bending modes [15,52]. However, in samples 2_Dublin and 3_Palermo the characteristic peaks of the lepidocrocite showed a higher relative intensity with respect to that of goethite, suggesting a higher relative amount of the former compound in these samples with respect to sample 1_Florence.

An intense shoulder at 1105 cm^{-1}, probably related to the Si-O-Si stretching absorption band, was observed in samples 2_Dublin and 3_Palermo (having high silicon content in the metallic substrates), suggesting the presence of silicon oxides [53]. Moreover, in sample 3_Palermo a pronounced shoulder at 560 cm^{-1} is observed that could indicate the presence of hematite in the corrosion layers.

In all spectra, a broad band in the range 2500-3600 cm^{-1} was found, with the main peak around 3200 cm^{-1} and shoulders around 3300 and 3500 cm^{-1}. This band is related to OH stretching of hydroxyl groups in the crystalline structures of both goethite and lepidocrocite, while the secondary peaks are related to various hydrogen bond types characterized by different bond coordination [54]. The OH bands related to water vibration in crystal structures also occur in this region and the presence of crystallization water in the corrosion products was confirmed by the presence of a peak at 1650 cm^{-1}. Finally, the DRIFT spectra also show traces of organic compounds (band at 2800-3000 cm^{-1} and peaks around 1480 and 1380 cm^{-1}), probably due to contamination.

Micro-Raman analyses were carried out on different areas of the corrosion product cross sections with the aim of characterizing the surface layer stratigraphy and assessing the effects of the alloying elements of the corrosion product composition. The identification of the different phases was performed on the basis of their characteristic wavenumbers, according to the information reported in Table 4.

Concerning sample 1_Florence, the results of micro-Raman analysis are shown in Fig. 6. Alternating layers composed by lepidocrocite (L) and by goethite (G) with lepidocrocite were identified in the corrosion products layer (points 1 and 2 in Fig. 6a and spectra 1 and 2 in Fig. 6b). In addition, the presence of akaganeite, β-FeOOH, (Fig. 6c), was observed in porous areas where VPSEM/EDS analysis detected high content of chloride (Fig. 6a, point 3: [Cl] = 2.5 wt.%). This phase is often observed as a corrosion product of iron in oxidizing environments in presence of chlorides [61,62]. In fact, its crystalline structure allows the incorporation of chloride ions and its formation is favored with respect to goethite and lepidocrocite, when ferrous hydroxychloride (β-$Fe_2(OH)_3Cl$), formed in chloride-rich environment, is oxidized [63,64].

The results of micro-Raman analyses carried out on the cross section of sample 2_Dublin are shown in Fig. 7. The results showed that the outer layer of corrosion products was composed of lepidocrocite (point 1 in Fig. 7a, spectrum 1 in Fig. 7b), while in the innermost layers the simultaneous presence of lepidocrocite and goethite was observed (point 2 in Fig. 7a, spectrum 2 in Fig. 7b). These results are in agreement with DRIFT analyses that highlighted the presence of both lepidocrocite and goethite in the whole corrosion product layer. Moreover, these findings are in agreement with the atmospheric corrosion models proposed in the literature that reports the transformation of the more reactive lepidocrocite, formed at short times on the artefact surface, in the more stable goethite after longer exposure periods [65] The VPSEM/EDS mapping carried out on the cross section of the sample 2_Dublin showed the presence of silicon in the corrosion products layer, more concentrated at the metal / corrosion interface (Fig. 4) and in some areas of the corroded layer. The micro-Raman analysis performed in the silicon-rich (about 3.8 wt.%) areas detected mainly goethite and lepidocrocite (point 3 in Fig. 7a, spectrum C in Fig. 7b) while the weak peaks around 870 and 990-1000 cm^{-1} could indicate the presence of amorphous silicon oxides (S), in agreement with DRIFT analyses.

Also on the sample 3_Palermo a corrosion product stratification was observed, with a silicon enrichment mainly localized at the metal / corrosion product interface, in the topotaxial layer and close to the graphite rosettes, and in some porous regions of the corrosion film (Fig. 4). Figure 8 shows the results of micro-Raman analyses carried out on the cross section of this sample. In the outer layer (point 1 in Fig. 8a, spectrum 1 in Fig. 8b), mainly hematite (H) and maghemite (γM) were detected while the presence of traces of goethite and lepidocrocite could be related to the shoulders at 388 and 373 cm^{-1}, respectively. In the inner layer (point 2 in Fig. 8a, spectrum 2 in Fig. 7c) still hematite and maghemite with traces of goethite and lepidocrocite were detected. The unusual intensity of hematite peak at 614 cm^{-1} could be related to the crystal orientation [66]. The Raman spectrum 3, in Fig. 8c, was collected in point 3 of Fig. 8a where the VPSEM/EDS analyses showed that the ratio between the atomic concentrations Fe / O is about 0.51. The intense peaks at around 378, 507, 643 and 720 cm^{-1} suggest the presence of maghemite, feroxyhyte / ferrihydrite, as well as traces of hematite [67].

3.3 Electrochemical characterization

Fig. 9 shows the EIS spectra, in Nyquist and Bode (log |Z| and phase angle vs. frequency) form, recorded on the samples 1_Florence, 2_Dublin and 3_Palermo. Apparently, they were characterized by two time constants, one corresponding to a well-defined capacitive loop at high frequencies (*hf*, $f > 10^2$ Hz) and the second one to a capacitive arc at low frequencies (*lf*, $f < 1$ Hz). However, these spectra were more closely fitted by a three time constant equivalent circuit, also including a middle frequency (*mf*) time constant in the frequency range

$1< f < 10^2$ Hz. The adopted equivalent circuit (EC) is reported in Fig. 10 and describes the behavior of an electrode covered by a porous film of corrosion products, where the substrate corrosion involves a diffusion step and a charge transfer process at the bottom of the film pores [37,68,69]. The EC is composed by a resistance, R_S, related to both the test electrolyte and the electrical connectors, in series with two nested parallel R-CPE couples, the first one in the *hf* range describing the dielectric properties of the surface film (R_f-CPE_f), while the second one in the *mf* range related to the charge transfer process at the pore bottom (R_{ct}-CPE_d). R_f and R_{ct} corresponded to the pore resistance and the charge transfer resistance respectively, while CPE_f and CPE_d were constant phase elements, used instead of the film and double layer capacitances, to fit the depressed capacitive arcs, caused by surface roughness and inhomogeneities. The impedance of CPE is given by:

$$Z = Y^{-1}(j\omega)^{-n} \quad (1)$$

where $\omega = 2\pi f$ is the angular frequency, $j = \sqrt{(-1)}$ is the imaginary unit, Y is a frequency independent value and n is a fit parameter with values in the range $0 \leq n \leq 1$, which measures the element deviation from the ideal capacitive behavior, characterized by n = 1. For n = 0, CPE is a pure resistor and for n = 0.5, CPE can model a diffusive process [70-72].
The *lf* portion of the spectra was best fitted by a generalized finite length Warburg element, W_s, introduced in series to the charge transfer resistance, R_{ct}, suggesting that both diffusion and charge transfer affect the substrate corrosion rate. The mathematical impedance expression of W_s is:

$$W_s = R_W \frac{tanh(j\omega T)^p}{(j\omega T)^p} \quad (2)$$

where T is a time constant, R_W is a resistance, and p is an exponent which can vary in the range $0 < p < 1$. For p = 0.5, $T = L^2 / D$, where L is the thickness of the diffusion layer and D is the diffusion coefficient [73].
In Table 5, the values of the parameters estimated by spectra fitting are reported together with the χ^2 parameter, which assess the good quality of the fitting, in the range $1.2\text{-}6.9 \cdot 10^{-3}$. For sample 2_Dublin, the Y_f values were rather low (about 0.1 $\mu\Omega^{-1}$ cm^{-2} s^n), while they were much higher in the case of samples 1_Florence (86 $\mu\Omega^{-1}$ cm^{-2} s^n) and 3_Palermo (4.3 $\mu\Omega^{-1}$ cm^{-2} s^n). In order to understand if these data match with patina thickness as evaluated by microscopic observations, the equation:

$$C_f = Y_f(\omega_m)^{n_f - 1} \quad (3)$$

was used to convert the Y_f parameters into the associated capacitances (where ω_m is the angular frequency at which the imaginary part of the impedance reaches a maximum and n_f, with values in the range 0.62-0.74, is the exponent in the CPE_f equation) [74-76]. The obtained C_f value for sample 2_Dublin is 0.006 $\mu\Omega^{-1}$ cm^{-2}, a common capacitance value for the corrosion product film, confirming the proper attribution of the *hf* capacitive loop to the film dielectric behavior [69,77,78]. However, as the film thickness estimated by VPSEM/EDS is about 40 μm, an even lower C_f value would be expected, on the basis of the equation:

$$C_f = \frac{A\varepsilon\varepsilon_0}{\delta} \quad (4)$$

where A is the exposed area of the test electrode, ε the dielectric constant of the oxide film, usually close to 10 [69], $\varepsilon_0 = 8.8542 \cdot 10^{-14}$ F cm^{-1} the vacuum permittivity and δ the thickness of the film). This is likely due to the high roughness of the film which determines a higher real oxide surface area. The C_f values of the samples 1_Florence and 3_Palermo were in the range 0.3-3 $\mu\Omega^{-1}$ cm^{-2} s, that is even higher than that of the sample 2_Dublin, in spite of their higher measured film thickness (in the range 115-130 μm). These high C_f values cannot be related to the dielectric properties of the whole films. Instead, as these films are affected by multiple cracks and pores, the values are likely related only to a thin inner adherent portion of the surface films [69]. The low R_f values (38 and 50 Ω cm^2 for the samples 1_Florence and 3_Palermo, much lower than that of the sample 2_Dublin, 1450 Ω cm^2) are compatible with the presence of these thin inner oxide layers.
In the *mf* range, the Y_d values are in the range 0.15-1.7 $m\Omega^{-1}$ cm^{-2} s^n which are common for charge transfer processes on rough metal / electrolyte interfaces [79-81]. In the case of 2_Dublin, the lowest Y_d values were obtained, likely due to the presence of a lower pore fraction in the surface patina. This hypothesis is supported by the presence of the highest R_{ct} and R_W values in this sample, suggesting relatively slow charge transfer and diffusion processes through the surface film. The rate of mass transport was found to significantly affect the

substrate corrosion, in agreement with the results of other research studies investigating the electrochemical behavior of heavily rusted carbon steel and cast iron samples [68,69,82]. In fact, for all samples R_W was always higher than R_{ct} and R_f.

The polarization resistance, R_p, values of the three samples, which are inversely proportional to the corrosion rates [83], can be calculated by the sum of the three resistance contributions: $R_p = R_f + R_{ct} + R_W$. They are reported in Table 5 and show that, as a consequence of a slow charge transfer and particularly diffusion process through a relatively homogeneous compact patina, the sample 2_Dublin undergoes a much lower corrosion rate (high R_p) than samples 1_Florence and 3_Palermo.

4 Conclusions

Our study investigates the state of conservation of three artefacts of historical street furniture in cast iron, dating back to the second half of nineteenth century and coming from foundries located in Italy, France and Great Britain. Although no information is available about the manufacturing techniques of the examined artefacts, the results showed that the composition of the alloys and their microstructural features (form, distribution and size of graphite, and microstructural constituents) were similar to those frequently encountered in complex shape castings with variable wall thickness.

The study of the patina stratification and the morphology of the corrosion attack evidenced the presence of a severe alloy graphitization. This phenomenon was accompanied by the formation of corrosion product layers of variable thickness (40 μm for the sample 2_Dublin and between 115 and 130 μm for the samples 1_Florence and 3_Palermo), containing mainly iron oxides, oxy-hydroxides and amorphous silicon oxides. In particular, the patinas on all samples contained lepidocrocite and goethite and, on the sample 3_Palermo, also hematite, maghemite and feroxyhyte / ferrihydrite. The sample 1_Florence, evidenced a significant contamination by chlorides associated to the presence of akaganeite.

The electrochemical characterization evidenced that the sample 2_Dublin was the most corrosion resistant, due to the presence of a relatively thin, but more compact film of corrosion products. Instead, the other two samples showed higher corrosion rates, due to the development of quite porous thick oxide films incapable to slow down the charge transfer and diffusion steps of the corrosion process. In sample 1_Florence, also chlorides and non-protective akaganeite likely contributed to impair the substrate corrosion resistance.

Acknowledgements

Dr. Raffaella Bassi Neri and Dr. Antonio Neri, NERI Foundation – The Italian Museum of Cast Iron (Longiano, FC, Italy), are gratefully acknowledged for providing the cast iron artefacts investigated in the present work.

References

1. R. Bassi, L. Bazzocchi, *Cast iron artefacts for city décor: a list of the principal typologies,* in: So light and yet a metal – The art of cast iron in the 19th and 20th centuries, edited by R. Bassi, C. Biasini Selvaggi, M.G. Massafra (Barbieri Selvaggi Editori, Manduria, 2011).
2. R. Bassi Neri, *La ghisa: quando il gusto incontrò l'arte industriale* (Arredo&Città, 2011).
3. J. Gay, *Cast iron: Architecture and ornament, Function and Fantasy* (John Murray Publishers Ltd., London, 1985).
4. M. Schumacher, *Seawater Corrosion Handbook* (Noyes Data Corporation, New Jersey, 1979).
5. G. Kreysa, R. Eckermann, *Dechema Corrosion Handbook*, Vol. **11** (VCH Publishers, New York, 1992).
6. A. Reynaud, *Corrosion of cast irons*, in: Shreir's Corrosion – Corrosion and degradation of engineering materials, edited by B. Cottis *et al.*, Vol. **3** (Elsevier Ltd., Amsterdam, 2010).
7. K. Kreislova, D. Knotkova, H. Geiplova, *Atmospheric corrosion of historical industrial structures,* in: Corrosion and conservation of cultural heritage metallic artefacts, edited by P. Dillmann *et al.* (Woodhead Publishing, Cambridge, 2013).
8. S. Godfrain, R. Pender, B. Martin, *English Heritage – Practical building conservation – Metals* (Ashgate Publishing Limited, Farnham, 2012).
9. P. Dillmann *et al.*, *Corrosion and conservation of cultural heritage metallic artefacts* (Woodhead Publishing, Cambridge, 2013).
10. M. Tsuda, Y. Murata, Imono **54**, 605 (1982).

11. T. Misawa *et al*, Corros. Sci. **14**, 279 (1974).
12. A. Raman, B. Kuban, K. Razvan, Corros. Sci. **32**, 1295 (1991).
13. S. Music, M. Gotic, S. Popovic, J. Mater. Sci. **28**, 5744 (1993).
14 A.V. Ramesh Kumar, R. Singh, R.K. Nigam, J. Radioanal. Nucl. Chem. **242**, 131 (1999).
15. P. Cambier, Clay Miner. **21**, 191 (1986).
16. T. Ishikawa *et al*, Corros. Sci. **40**, 1239 (1998).
17. R. Balasubramaniam, A.V. Ramesh Kumar, Corros. Sci. **42**, 2085 (2000).
18. Y.Y. Chen *et al.*, Corros. Sci. **47**, 1001 (2005).
19. M. Natesan, G. Venkatachari, N. Palaniswamy, Corros. Sci. **48**, 3584 (2006).
20. T. Shinohara, S. Motoda, W. Oshikawa, Mater. Sci. Forum **475–479**, 61 (2005).
21. I. Shitanda *et al.*, Sens. Actuators B **139**, 292 (2009).
22. F. Zucchi *et al.*, J. Appl. Electrochem. **36**, 195 (2006).
23. C. Monticelli *et al.*, Cem. Concr. Res. **87**, 53 (2016).
24. F. Zucchi *et al.*, Mater. Corros. **60**, 199 (2009).
25. A. Frignani *et al.*, Corros. Sci. **63**, 29 (2012).
26. A. Balbo *et al.*, Corros. Sci. **73**, 80 (2013).
27. M. Albini *et al.*, Mater. Corros. **67**, 200 (2016).
28. B. Ramirez Barat *et al.*, ChemElectroChem **5**, 2698 (2018).
29. A. Balbo *et al.*, Corros. Sci. **59**, 204 (2012).
30. C. Chiavari *et al.*, Prog. Org. Coat. **82**, 91 (2015).
31. G. Masi, Prog. Org. Coat. **127**, 286 (2019).
32. C. Chiavari *et al.*, Corros. Sci. **100**, 435 (2015).
33. M. Albini *et al.*, Corros. Sci. **143**, 84 (2018).
34. C. Monticelli *et al.*, Corros. Sci. 148, 144 (2019).
35. P. Letardi, *Proceedings of Metal 2004, National Museum of Australia, Canberra, ACT, 2004*.
36. P. Letardi, *Misure elettrochimiche per la caratterizzazione e il monitoraggio del potere protettivo di patine e rivestimenti: la tecnica EIS*, in: Monumenti in bronzo all'aperto, edited by P. Letardi, I. Trentin, G. Cutugno (Nardini, Firenze, 2004).
37. E. Angelini *et al.*, Int. J. Circ. Syst. Signal Process. **8**, 240 (2014).
38. A. Balbo *et al.*, *Proceedings of EUROCORR 2014, European Federation of Corrosion Event No. 364, Pisa, 2014*, Paper 7259.
39. B. Ramirez Barat *et al.*, Electrochim. Acta **182**, 751 (2015).
40. B. Ramirez Barat *et al.*, Sens. Actuators B **261**, 572 (2018).
41. S. Grassini *et al.*, Measurement **114**, 508 (2018).
42. C. Soffritti *et al.*, Metall. Ital. **4**, 5 (2018).
43. J.R. Davis, *ASM Specialty Handbook, Cast Irons* (ASM International, Materials Park, OH, 1996).
44. Standard EN ISO 945-1:2008 *"Microstructure of cast iron – Part 1: Graphite classification by visual analysis"*.
45. A.A. Pereira, L. Boehs, W.L. Guesser, J. Mater. Process. Tech. **179**, 165 (2006).
46. J. Lacaze *et al.*, Advances in Materials Science and Engineering, Article ID 638451 (2013).
47. A. Sommerfeld, B. Tonn, Int. J. Met. **3**, 39 (2009).
48. A.C. de Ruggiero *et al.*, Mater. Sci. Forum **941**, 663 (2018).
49. Y.S. Lerner, J. Mater. Eng. Perform. **12**, 141 (2003).
50. J. Aramendia *et al.*, J. Raman Spectrosc. **43**, 1111 (2012).
51. S. Nowak *et al.*, Talanta **186**, 133 (2018).
52. S. Rahimi *et al.*, J. Ind. Eng. Chem. **23**, 33 (2015).
53. D. Lin-Vien *et al.*, *The handbook of infrared and raman characteristic frequencies of organic molecules* (Academic press, Cambridge, Massachusetts, 1991).
54. J.J Max *et al.*, J. Chem. Phys. **126**, 184507 (2007).
55. D.L.A. de Faria, S. Venâncio Silva, M.T. de Oliveira, J. Raman Spectrosc. **28**, 873 (1997).
56. B. Lafuente *et al.*, *The power of databases: the RRUFF project*, in: Highlights in Mineralogical Crystallography, edited by T. Armbruster, R.M. Danisi (De Gruyter, Berlin, 2015).
57. Y. El Mendili *et al.*, Corros. Sci. **88**, 56 (2014).
58. S. Reguer *et al.*, Nucl. Instrum. Methods Phys. Res. B **240**, 500 (2005).
59. D. Neff *et al.*, J. Raman Spectrosc. **37**, 1228 (2006).

60. P. Colomban, *Potential and drawbacks of Raman (micro)spectrometry for the understanding of iron and steel corrosion,* New trends and developments in automotive system engineering Marcello Chiaberge, IntechOpen, (2011) DOI: 10.5772/13436.
61. F.R. Pérez, C.A. Barrero, K.E. García, Corros. Sci. **52**, 2582 (2010).
62. J. Monnier *et al.*, Corros. Sci. **52**, 695 (2010).
63. P. Refait, J.-M.R. Génin, Corros. Sci. **39**, 539 (1997).
64. C. Remazeilles, P. Refait, Corros. Sci. **49**, 844 (2007).
65. M. Yamashita *et al.*, Corros. Sci. **36**, 283 (1994).
66. D. Bersani, P.P. Lottici, A. Montenero, J. Raman Spectrosc. **30**, 355 (1999).
67. J. Monnier *et al.*, Appl. Phys. A **99**, 399 (2010).
68. L. Bousselmi *et al.*, Corros. Sci. **39**, 1711 (1997).
69. M. Sancy *et al.*, Corr. Sci. **52**, 1222 (2010).
70. E. Barsoukov, J.R. Macdonald, *Impedance spectroscopy* (John Wiley & Sons, Inc., New York, 1987).
71. J.B. Jorcin *et al.*, Electrochim. Acta **51**, 1473 (2006).
72. C.H. Hsu, F. Mansfeld, Corros. **57**, 747 (2001).
73. G. Trabanelli *et al.*, Cem. Concr. Res. **35**, 1804 (2005).
74. Y. Huang, H. Shih, F. Mansfeld, Mater. Corros. **61**, 302 (2010).
75. A. Frignani *et al.*, Mater. Corros. **62**, 995 (2011).
76. F. Zanotto *et al.*, Mater. Chem. Phys. **129**, 1 (2011).
77. M.E. Orazem, B. Tribollet, *Electrochemical impedance spectroscopy*, (John Wiley & Sons, Inc., New York, 2008).
78. G. Hao *et al.*, Trans. Tianjin Univ. **22**, 516 (2016).
79. F. Batmanghelich, L. Li, Y. Seo, Corros. Sci. **121**, 94 (2017).
80. S. Sun *et al.*, Colloids Surf., A **558**, 130 (2018).
81. X. Zhang *et al.*, Corros. Sci. **82**, 165 (2014).
82. O.E. Barcia *et al.*, Electrochim. Acta **47**, 2109 (2002).
83. M. Stern, A.L. Geary, J. Electrochem. Soc. **104**, 56 (1957).

FIGURE CAPTIONS

Fig. 1 – Optical micrographs of the microstructure observed on the cross sections of cast ironggieros: sample 1_Florence (a) before and (d) after chemical etching; sample 2_Dublin (b) before and (e) after chemical etching; sample 3_Palermo (c) before and (f) after chemical etching.

Fig. 2 – VPSEM micrographs of the corroded surfaces of cast irons: (a) sample 1_Florence; (b) sample 2_Dublin; (c) sample 3_Palermo.

Fig. 3 – VPSEM backscattered electron images of the stratigraphy of the corrosion patina observed on the cross sections of the artefacts: (a) sample 1_Florence; (b) sample 2_Dublin; (c) sample 3_Palermo.

Fig. 4 – VPSEM/EDS backscattered electron images and maps of elemental distribution in the corrosion layers on the cross sections of the examined samples.

Fig. 5 – DRIFT spectra of the collected samples.

Fig. 6 – Micro-Raman analysis on the cross section of the sample 1_Florence: (a) investigated areas; (b) and (c) Raman spectra.

Fig. 7 – Micro-Raman analysis on the cross section of the sample 2_Dublin: (a) investigated areas; (b) Raman spectra.

Fig. 8 – Micro-Raman analysis on the cross section of the sample 3_Palermo: (a) investigated areas; (b) and (c) Raman spectra.

Fig. 9 – EIS spectra, in Nyquist (a) and Bode (b, c) form, recorded on the samples 1_Florence, 2_Dublin and 3_Palermo.

Fig. 10 – Equivalent circuit (EC) used to analyze the EIS spectra.

Table 1 – Summary of fragments, together with information on origin, year of manufacturing and nationality of the foundry.

Fragment	Origin	Year of manufacturing	Nationality of the foundry
1_Florence	Column of balustrade at Piazzale Michelangelo (Florence, Italy)	1850-1860	Italy
2_Dublin	Street lamp post at O'Connell Bridge (Dublin, Ireland)	1870	France
3_Palermo	Street lamp post base at Palermo (Italy)	1880-1890	Great Britain

Table 2 – Semi-quantitative elemental composition (wt.%) of wide areas (1.0 × 0.5 mm^2) of alloys in the artefacts, measured by VPSEM/EDS. Carbon was overrated due to the physical background of the technique; accordingly, the percentages are representative of the compositions of the alloys except the graphite lamellae.

Sample	Si	P	S	Ti	Mn	Fe
1_Florence	0.72	0.09	0.12	0.04	0.13	98.9
2_Dublin	2.4	1.5	0.15	0.15	0.55	95.3
3_Palermo	2.9	1.06	0.43	0.20	1.7	93.7

Table 3 – Semi-quantitative elemental surface composition (wt.%) of wide areas (1.0 × 0.5 mm^2) of the corrosion product patinas, measured by VPSEM/EDS.

Sample	C	O	Al	Si	P	S	K	Ca	Cl	Fe	Zn	Pb
1_Florence	19.95	28.13	-	0.35	0.06	0.11	-	0.28	0.61	50.51	-	-
2_Dublin	13.94	28.89	1.10	3.05	0.38	0.16	0.24	0.43	0.05	44.15	3.74	3.87
3_Palermo	10.74	29.73	1.22	3.28	0.37	0.21	0.28	0.59	0.02	51.33	1.09	1.14

Table 4 – Raman characteristics wavenumbers of the main iron corrosion products (s: strong; m: medium; w. weak).

Compounds	Formula	Characteristic Wavenumber (cm^{-1})	Refs.
Goethite	α-FeOOH	248m, 299s, 390s, 479w, 533mw	[55], [56]
Akaganeite	β-FeOOH	308m, 390mw, 353w 720s	[57], [58]
Lepidocrocite	γ-FeOOH	220w, 248s, 299m, 375s, 525m, 645w	[55], [56]
Hematite	α-Fe_2O_3	225m, 247w, 292s, 412m, 495w613m	[55]
Maghemite	γ -Fe_2O_3	350-380, 460, 500, 643-670s, 715-720s	[55], [59]
Ferrihydrite	$Fe_2O_3x0,5H_2O$	350, ~ 510, ~710, ~1380	[59], [60]
Magnetite	Fe_3O_4	662s, 533w, 302w	[55]

Table 5 – Parameters obtained from EIS fitting with the adopted EC, together with the χ^2 parameter.

Sample	R_f (Ω cm^2)	Y_f (μΩ^{-1} cm^{-2} s^n)	R_{ct} (kΩ cm^2)	Y_d (μΩ^{-1} cm^{-2} s^n)	R_W (kΩ cm^2)	R_p (kΩ cm^2)	χ^2
1_Florence	38 ± 15	86 ± 11	0.13 ± 0.02	1660 ± 310	6.02 ± 0.59	6.19 ± 0.27	$5.2 \cdot 10^{-3}$
2_Dublin	1450 ± 93	0.10 ± 0.04	6.03 ± 0.82	150 ± 27	26.0 ± 3.6	33.5 ± 1.8	$6.9 \cdot 10^{-3}$
3_Palermo	50 ± 12	4.3 ± 1.5	1.22 ± 0.33	290 ± 69	5.70 ± 0.95	7.0 ± 1.0	$1.2 \cdot 10^{-3}$

Fig. 1

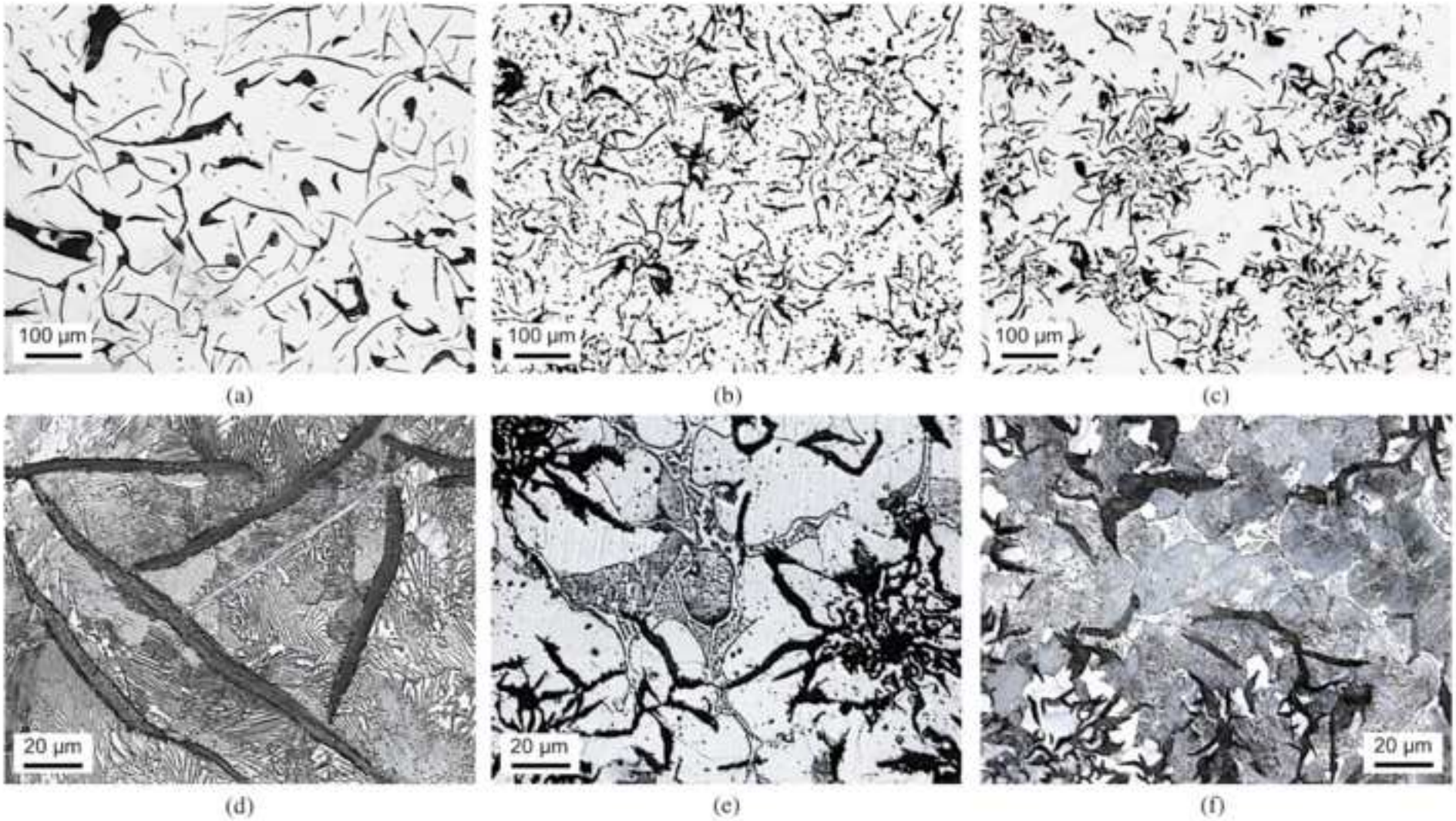

Fig. 2

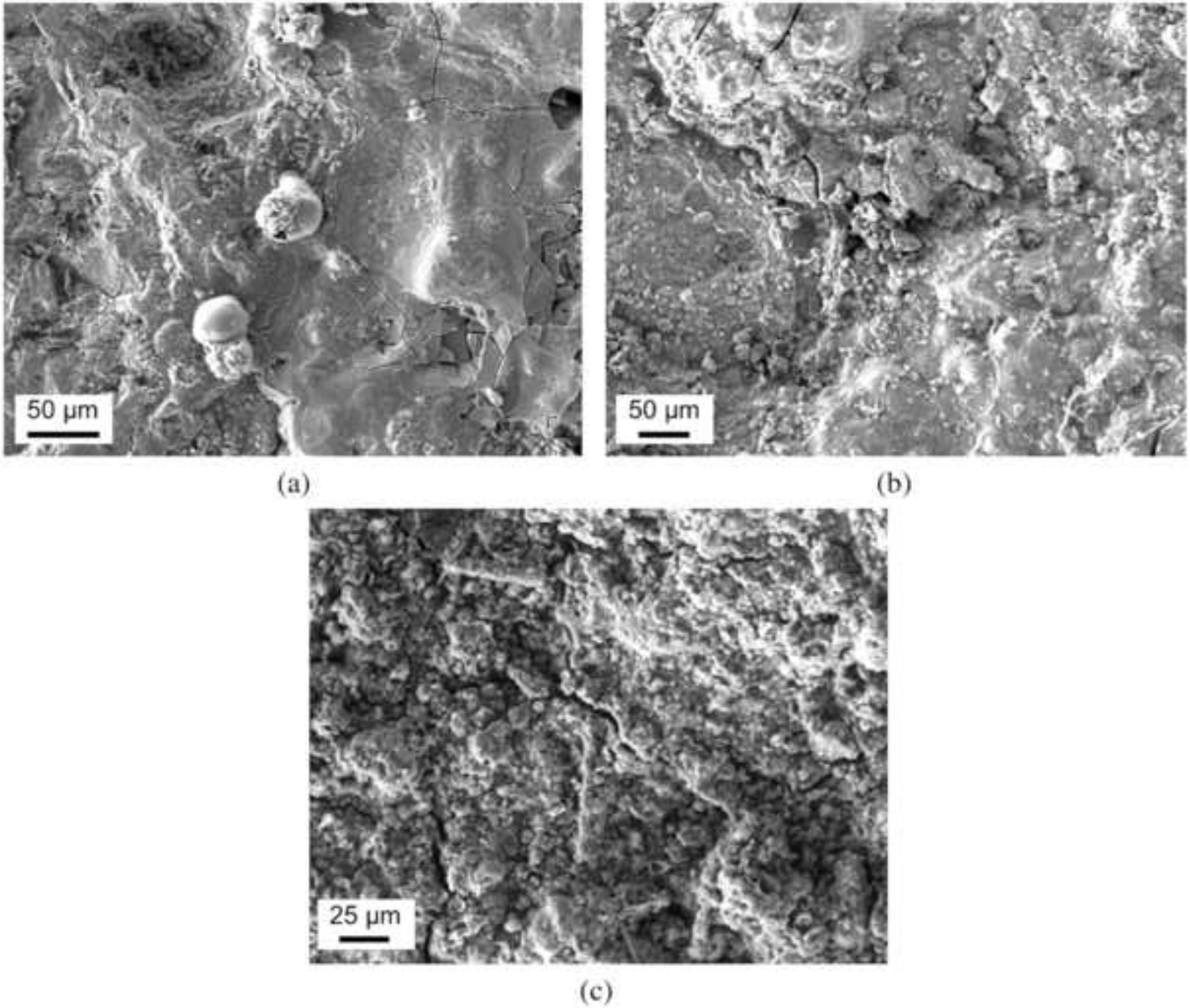

Fig. 3

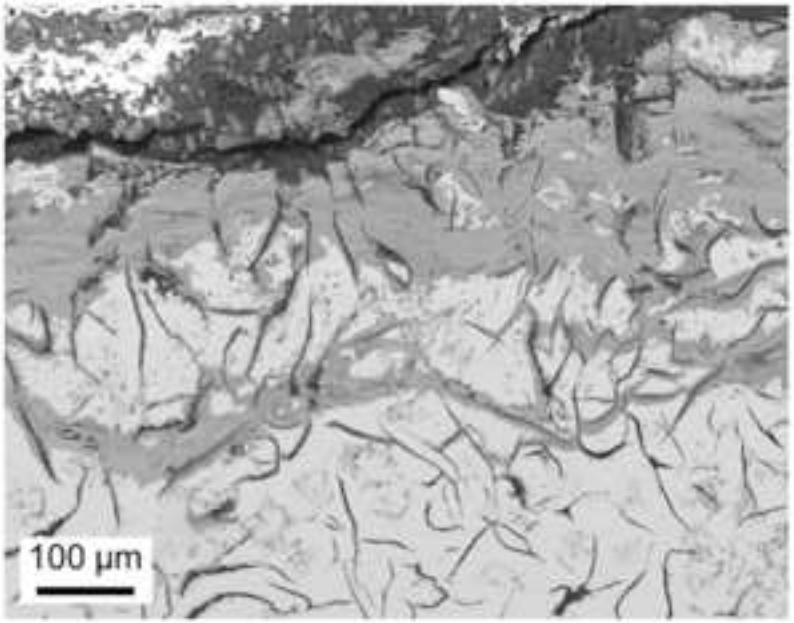

(a)

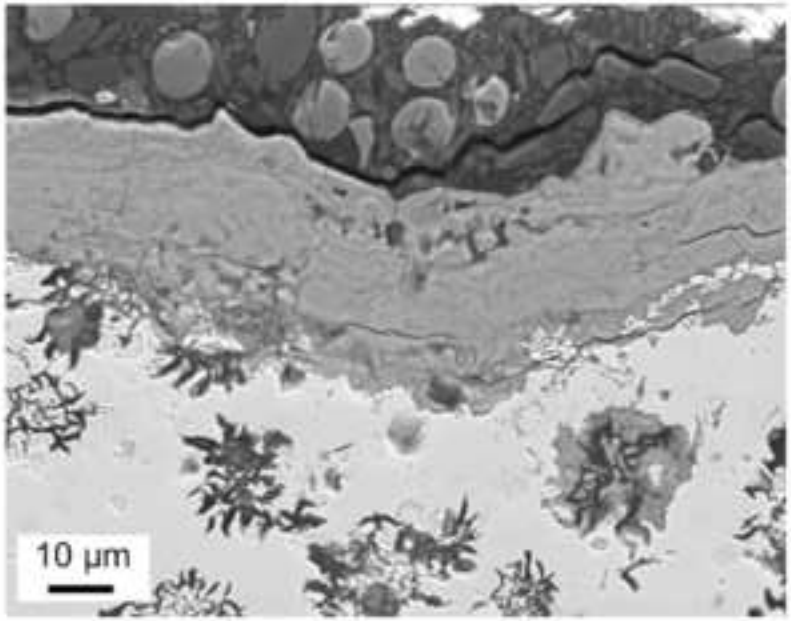

(b)

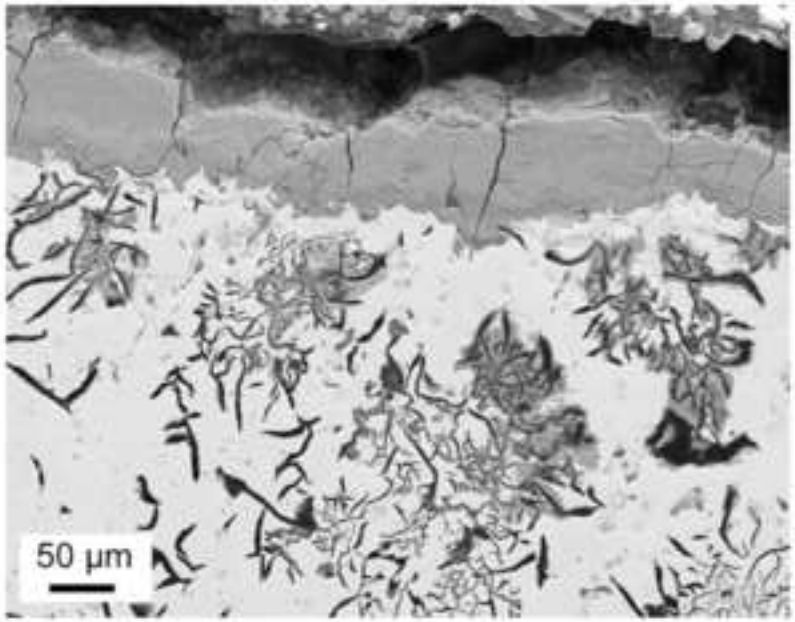

(c)

Fig. 4

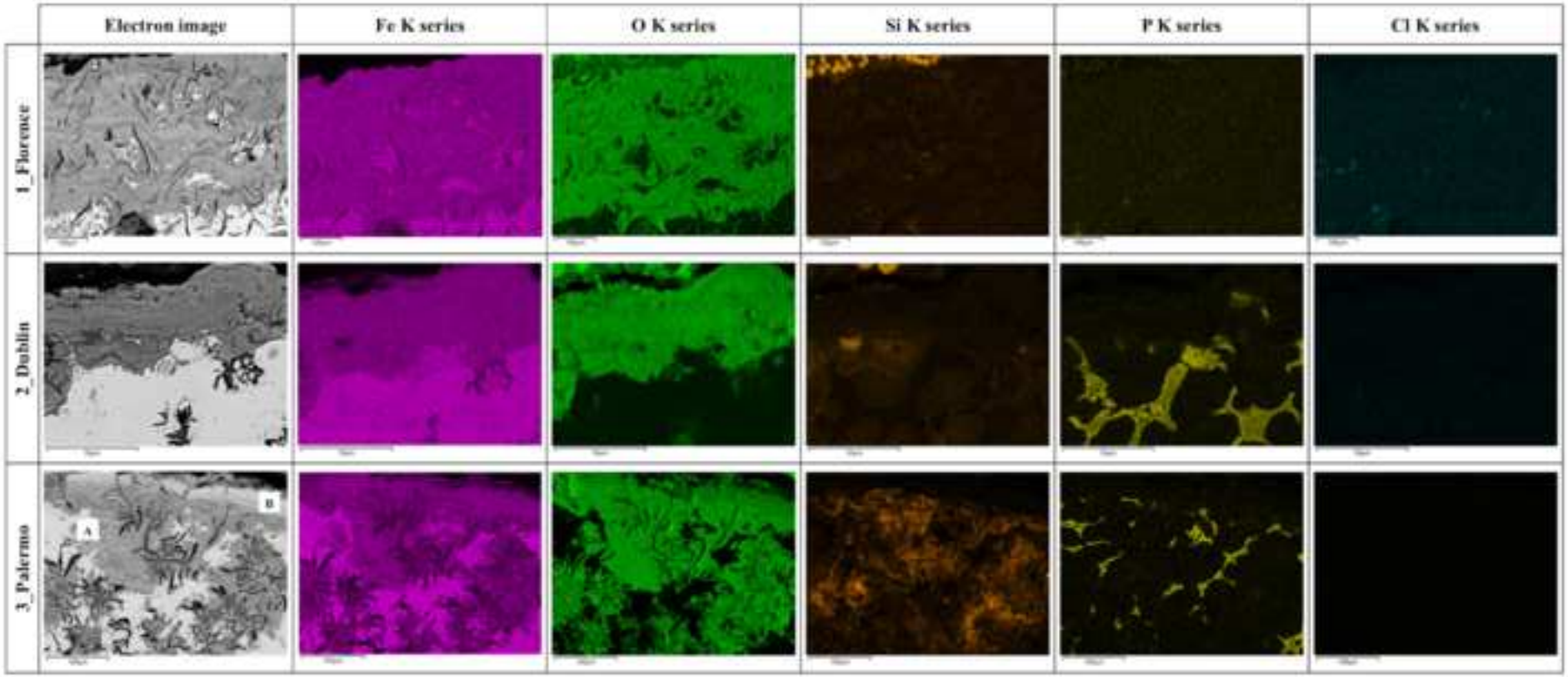

Fig. 5

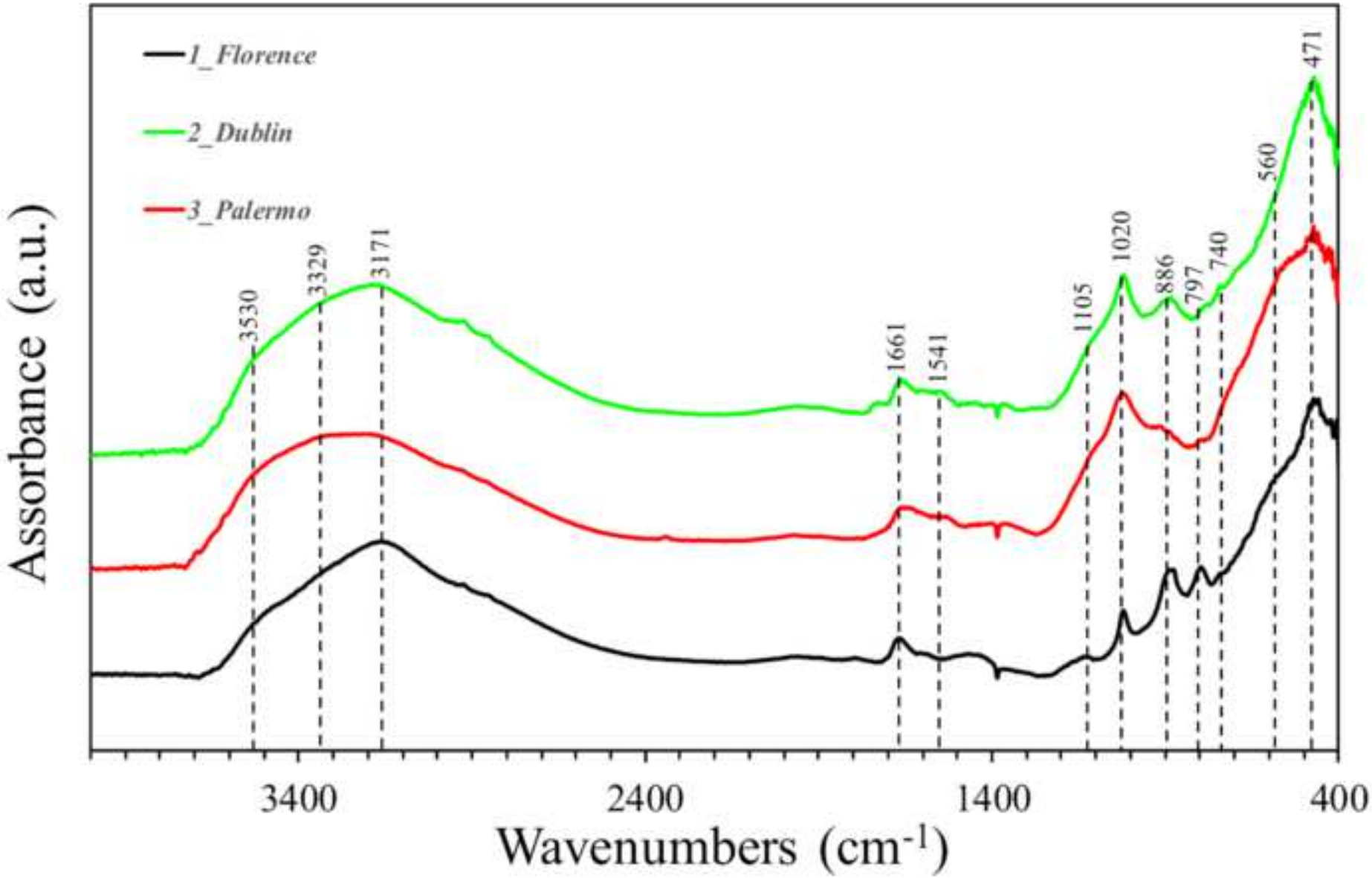

Fig. 6

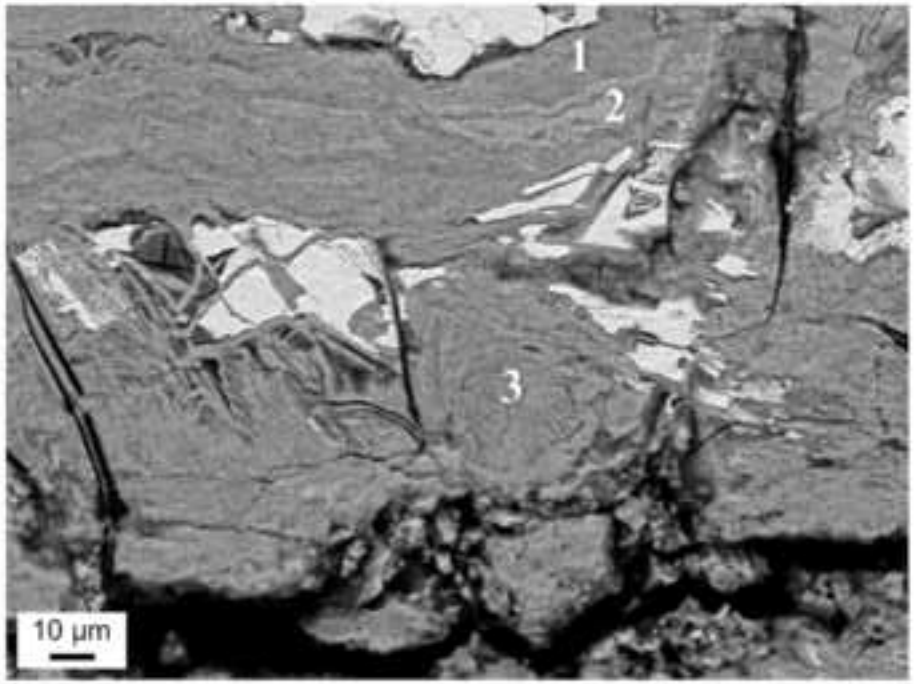

(a)

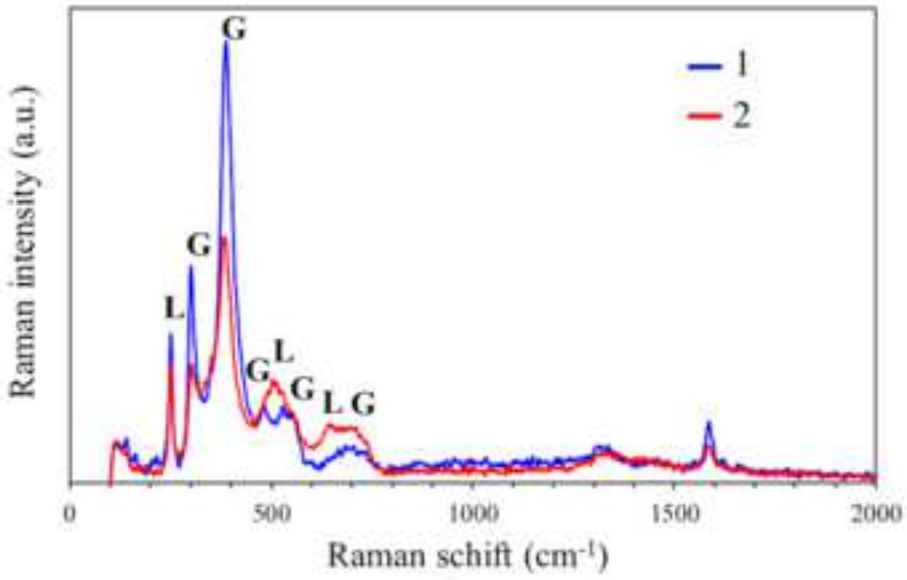

(b)

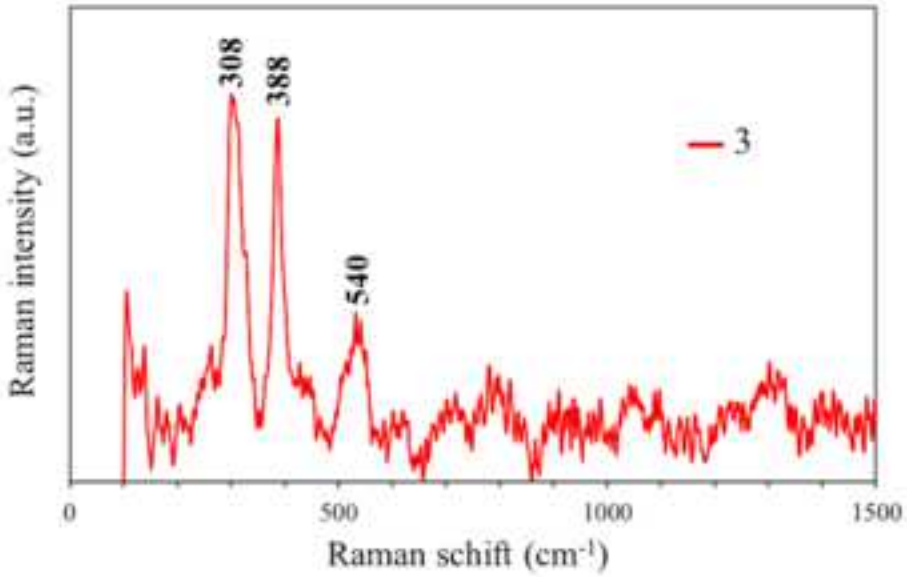

(c)

Fig. 7

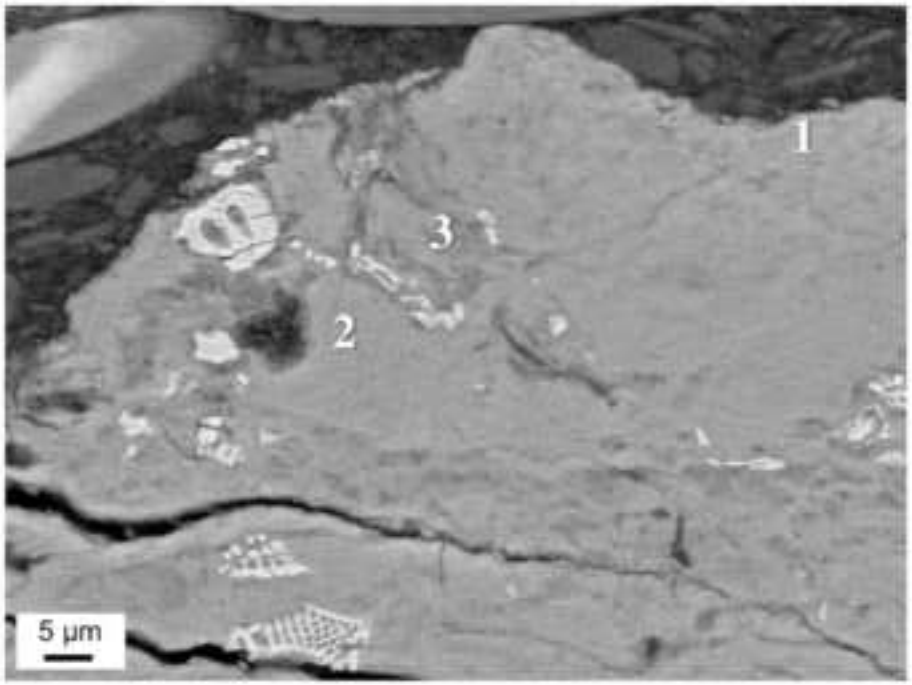

(a)

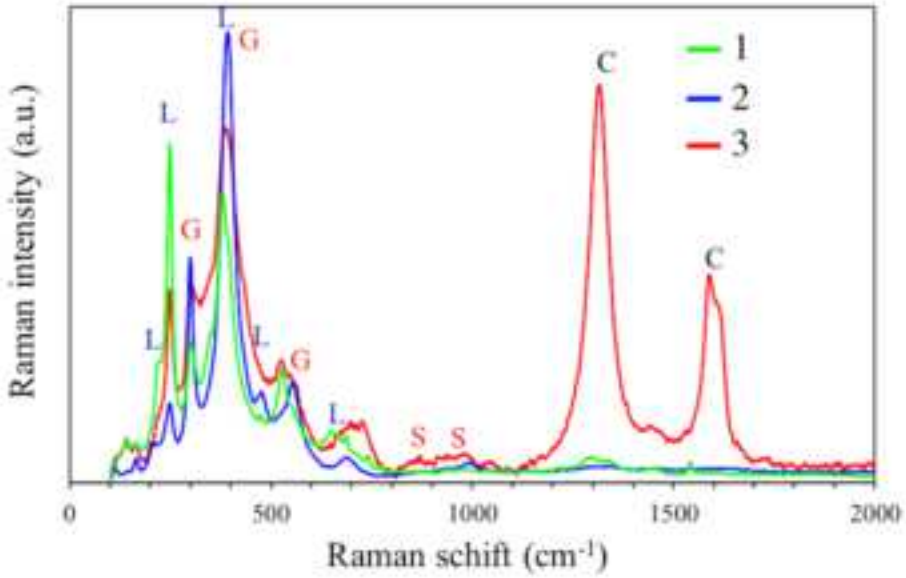

(b)

Fig. 8

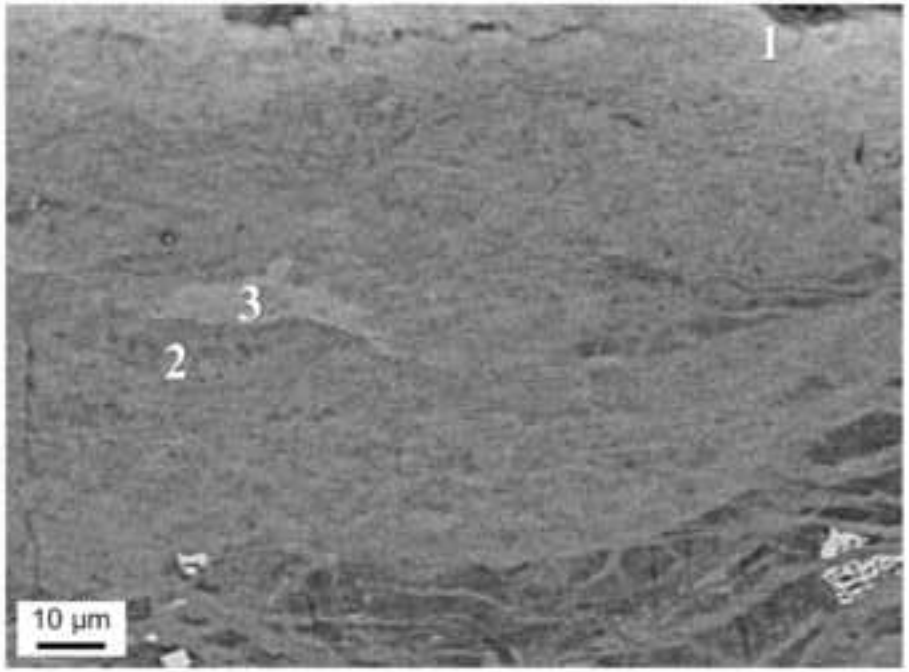

(a)

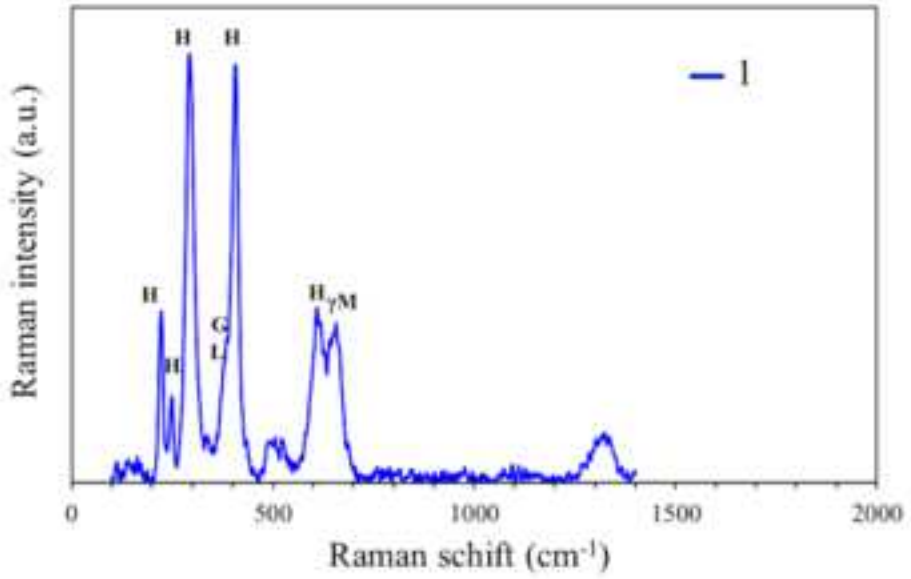

(b)

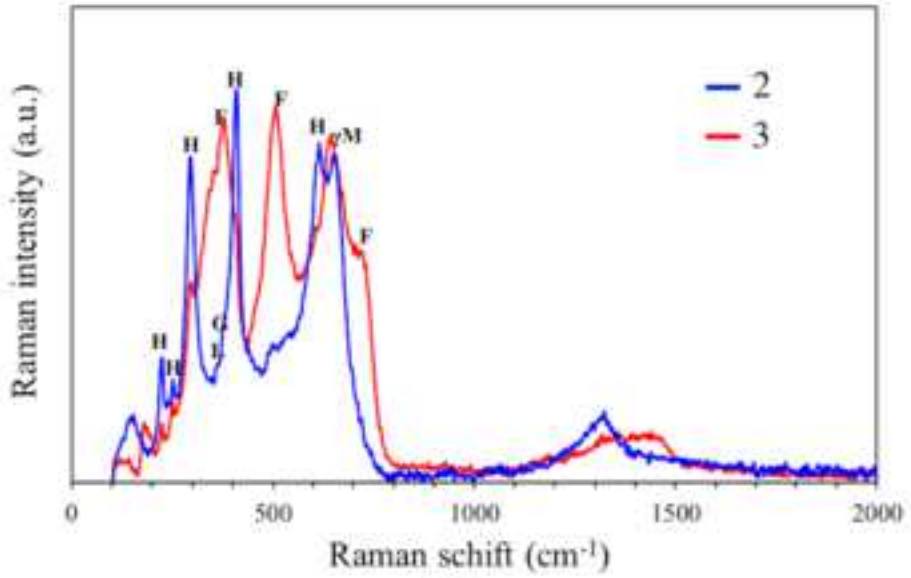

(c)

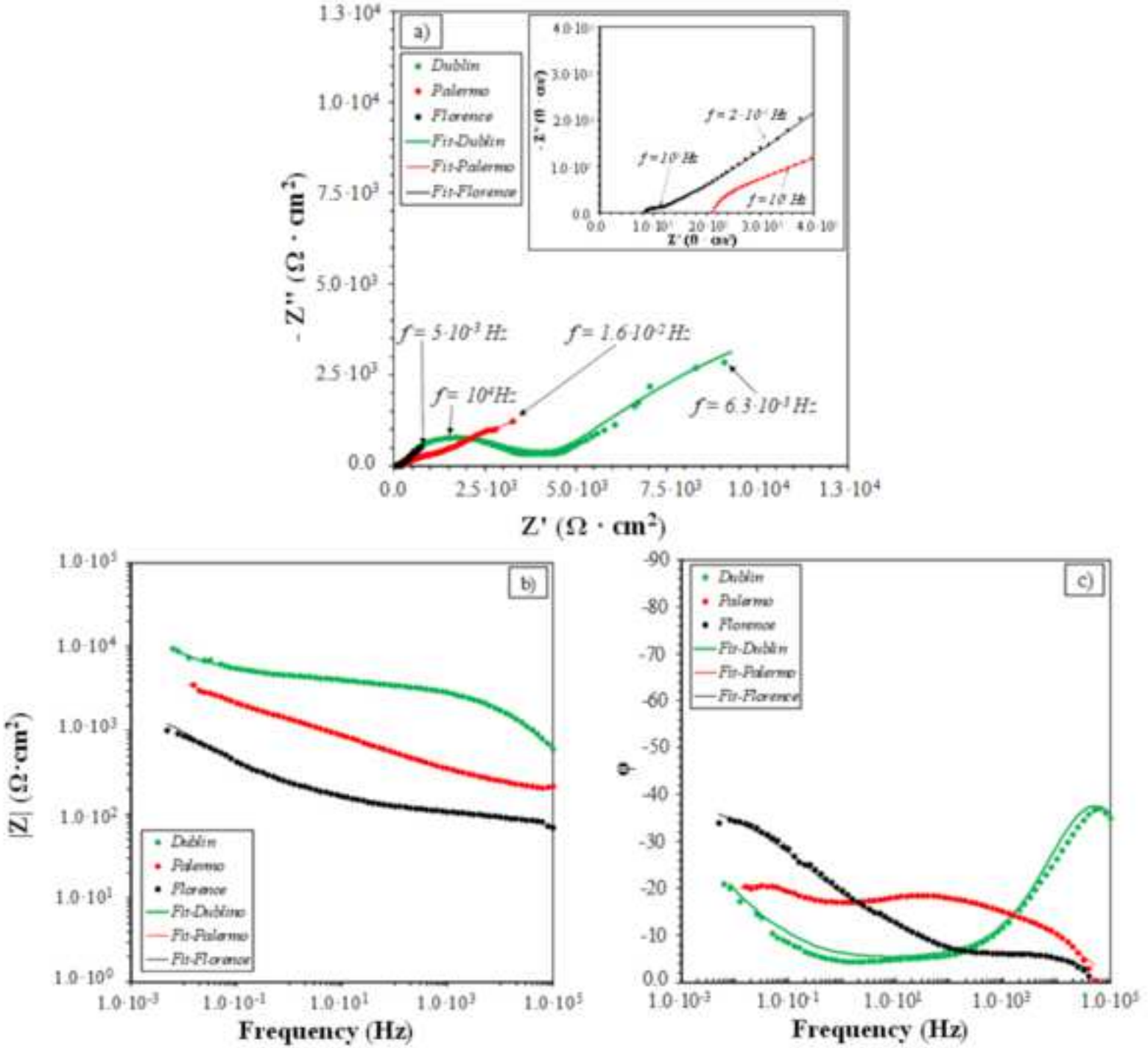

Fig. 10